Research Square

Preprints are preliminary reports that have not undergone peer review.
They should not be considered conclusive, used to inform clinical practice,
or referenced by the media as validated information.

In Vivo Cardiac Biomechanical Model Parameter Estimation from Ultrafast Shear Wave Elastography

Camilla Ferrario
Inria at Université Côte d'Azur
Maelys Venet
Centre Hospitalier Universitaire de Bordeaux
Olivier Villemain
Centre Hospitalier Universitaire de Bordeaux
Maxime Sermesant
maxime.sermesant@inria.fr

Inria at Université Côte d'Azur

Research Article

Keywords: Cardiac mechanics, reduced-order electromechanics (0D), ultrafast ultrasound imaging, myocardial stiffness, patient-specific modeling, Bayesian calibration

Posted Date: February 25th, 2026

DOI: https://doi.org/10.21203/rs.3.rs-8744899/v1

License: This work is licensed under a Creative Commons Attribution 4.0 International License.
Read Full License

Additional Declarations: No competing interests reported.

In Vivo Cardiac Biomechanical Model Parameter Estimation from Ultrafast Shear Wave Elastography

Camilla Ferrario[1,3*], Maelys Venet[2], Olivier Villemain[2], Maxime Sermesant[1,3*]

[1]Epione Team, Inria at Université Côte d'Azur, Sophia Antipolis, France.
[2]Bordeaux University Hospital (CHU), Bordeaux, France.
[3]IHU Liryc, Electrophysiology and Heart Modeling Institute, Pessac, France.

*Corresponding author(s). E-mail(s): camilla.ferrario@inria.fr;
maxime.sermesant@inria.fr;

Abstract

Quantifying myocardial stiffness (MS) over the full cardiac cycle offers a direct window into tissue structure and mechanics, yet translating time-resolved shear wave elastography (SWE) into intrinsic material properties remains a complex inverse problem. While SWE provides detailed stiffness quantification, these measurements combine passive structural properties with active contractility under subject-specific loading conditions. In this work, we present a computational framework to decompose these contributions using a closed-loop reduced-order electromechanical model. We formulate the personalization process as a sequential inverse problem: first, a passive hyperelastic baseline is identified from the late-diastolic window; second, active contractile parameters are estimated by fitting the full-cycle waveform using a regularized covariance matrix adaptation evolution strategy (CMA-ES). We validated this framework on a cohort of healthy pediatric volunteers (n=20). The personalized models reproduced subject-specific stiffness trajectories with high fidelity (median cross-correlation 0.997, nRMSE 1.02). Uncertainty analysis confirmed the practical identifiability of the active parameters, with stable convergence across random initializations. This study establishes a computationally efficient, robust pipeline for converting non-invasive SWE assessments into interpretable mechanical signatures, paving the way for physics-informed phenotyping in clinical cohorts.

Keywords: Cardiac mechanics, reduced-order electromechanics (0D), ultrafast ultrasound imaging, myocardial stiffness, patient-specific modeling, Bayesian calibration.

1 Introduction

Characterizing the time-resolved mechanical state of the myocardium is essential for understanding cardiac function (Sermesant et al. 2011; Muslov et al. 2023). Unlike global pump metrics (e.g., ejection fraction or pressure-volume loops), which reflect the combined effect of tissue mechanics and loading, myocardial stiffness (MS) directly quantifies the intrinsic tissue's resistance to deformation and thus provides a mechanistically grounded descriptor of ventricular function.

The myocardium is a composite material with non-linear passive hyperelastic behavior and a time-varying active contractile response (Sagawa et al. 1977; Villalobos Lizardi et al. 2022). As a result, *in vivo* stiffness reflects both intrinsic constitutive properties and contractility, making it difficult to disentangle passive remodeling from

active tone. Decoupling these active and passive states remains a central challenge in cardiac biomechanics (Villalobos Lizardi et al. 2022; Villemain et al. 2019, 2020; Pernot et al. 2011).

Recent advances in ultrafast ultrasound imaging (UUI) have enabled the measurement of shear wave elastography (SWE) at high frame rates ($>$ 10 000 fps), allowing for the capture of transient shear wave propagation throughout the full cardiac cycle (Villalobos Lizardi et al. 2022; Cikes et al. 2014; Villemain et al. 2020; Caenen et al. 2024). In theory, these shear wave velocity variations through the cardiac cycle provide a direct signature of the changing mechanical state of the tissue (Caenen et al. 2024). However, translating non-invasive SWE measurements into interpretable material parameters poses a complex inverse problem. The stiffness measured by SWE is a combination of the passive extracellular matrix properties, the instantaneous density of attached actin-myosin cross-bridges, and the active contractility induced by molecular and structural changes in systole (Guccione et al. 1993). Consequently, raw SWE data alone cannot uniquely distinguish between passive remodeling and alterations in active contractility (Pernot et al. 2011).

In this work, we formulate the mapping from full-cardiac SWE stiffness assessments to subject-specific mechanical parameters as a regularized inverse problem solved with a computationally efficient reduced-order (0D) electromechanical model (EM) to simulate the global dynamics of the myocardium. While 3D finite element models offer high spatial resolution, their computational cost prohibits the iterative solving required for robust uncertainty quantification and parameter identification in clinical cohorts. Conversely, 0D formulations preserve the essential thermodynamical consistency and physiological coupling between circulation and myocardial mechanics while remaining computationally efficient (Caruel et al. 2013; Bestel et al. 2001; Chapelle et al. 2012).

Building on our previous framework (Ferrario et al. 2025), we propose a sequential calibration pipeline that decomposes the total MS into its active and passive components (see Fig. 1). To mitigate parameter identifiability issues inherent in cardiac modeling (Villaverde et al. 2019), we cast personalization as a *multi-stage inverse problem* and extend the methodology in three key directions.

First, we isolate the passive properties by identifying a late-diastolic baseline using a hyperelastic-derived stretch shape function. This explicitly constrains the passive stiffness parameter, preventing baseline stiffness or diastolic stiffening from being absorbed into the active parameters (Pernot et al. 2011).

Second, we formulate the subsequent active personalization as a Bayesian maximum a posteriori (MAP) problem optimized with CMA-ES (Hansen 2007, 2023). Regularization is enforced through a population-based log-Gaussian prior, which stabilizes poorly informed directions while preserving inter-subject variability (Chabiniok et al. 2016; Molléro et al. 2018).

Third, within this probabilistic framework, we explicitly estimate the active stiffness scale k_0 in addition to activation and relaxation rates (k_{ATP}, k_{SR}) by fitting the residual active target over the full cardiac cycle.

The framework is validated on a cohort of healthy pediatric volunteers ($n = 20$), demonstrating feasibility, optimization stability and practical identifiability through uncertainty analysis across multiple random initializations.

2 Materials and Methods

This section describes the pipeline used to quantify MS and personalize the model. We first outline the SWE acquisition protocol and the clinical cohort. Then, we present the 0D-EM formulation and the myocardial tissue model. Finally, we detail the calibration linking model parameters to subject-specific clinical measurements.

2.1 Shear Wave Elastography Acquisition

SWE is an ultrafast ultrasound imaging (UUI) technique that tracks the propagation of transient shear waves (SWs) in the myocardium to estimate stiffness. UUI captures short-lived mechanical events that are not accessible with conventional echocardiography (Villemain et al. 2019; Pernot et al. 2011).

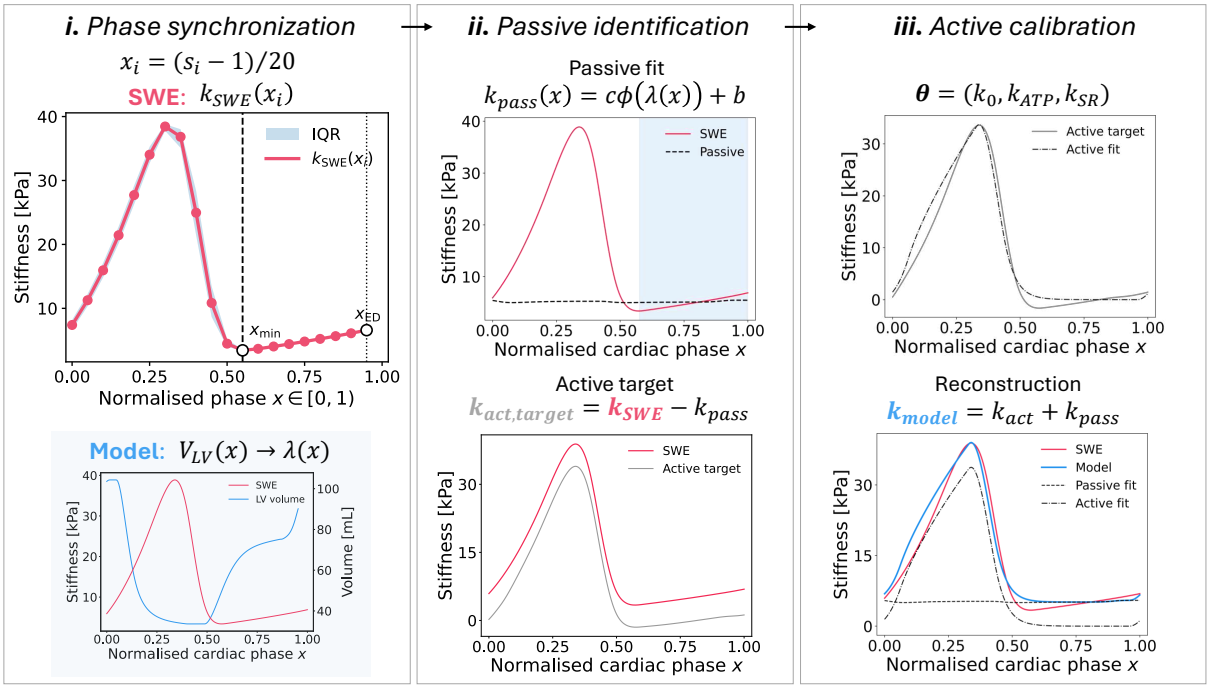


Fig. 1: Graphical overview of the calibration workflow. Cycle-resolved SWE stiffness (20 ECG-gated phases) is aligned with the last simulated cycle of the 0D-EM model on a normalised phase axis. Passive stiffness is identified in late diastole and subtracted to define the active target; active parameters are estimated with CMA-ES. Total stiffness is reconstructed as the sum of passive and active components.

Cardiac SWE can be performed either by externally generating SWs using acoustic radiation force (ARF) or by exploiting spontaneous waves triggered by physiological transients, such as valve closure. Since our dataset was acquired with an ARF-based protocol, we briefly summarise that approach and refer Villemain et al. (2020, 2019); Malik et al. (2024); Venet et al. (2025) for broader methodological comparisons.

In this study, acquisitions were performed on a Verasonics Vantage system (*Verasonic Inc., Kirkland, WA, USA*) with a phased-array probe (6S-D, General Electric®). A focused ARF push (4 MHz, 300 µs, f-number 1) was applied to the antero-septal basal segment of the interventricular septum in a parasternal long-axis view. In response to that transient mechanical excitation, a SW was generated in the low–kHz-frequency range and propagated in the myocardium at velocities from 1 to 10 m/s, depending upon the intrinsic tissue stiffness. Tissue velocity maps were computed offline for each frame by using in-phase quadrature frame to frame cross-correlation, as illustrated in Fig. 2. Myocardial wall motion was removed by subtraction of the average wall motion during the acquisition, bringing to light tissue motion induced solely by the shear wave. SW velocity was computed at the depth of the mid-wall myocardium using spatiotemporal data from wave propagation. Finally the shear modulus μ (i.e. stiffness) was derived using the equation:

$$\mu \approx \rho\, c_s^2,$$

where c is the shear wave velocity and ρ is the volume mass of the tissue ($\rho \approx 1000$ kg m^{-3}). For each subject, measurements were collected at 20 ECG phases uniformly sampling the normalised R-R interval. Additional acquisition details are reported in Villemain et al. (2019, 2020), Malik et al. (2024) and Venet et al. (2025).

2.2 Dataset

The study population is derived from a prospective cohort of children and adolescents (<

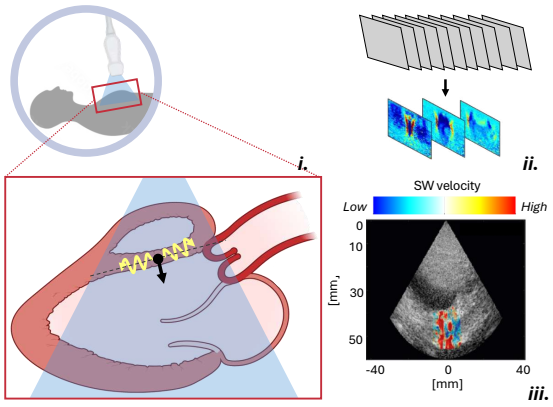


Fig. 2: SWE acquisition pipeline. The process includes (i) acoustic radiation force excitation, (ii) ultrafast plane-wave tracking, and (iii) myocardial shear wave (SW) velocity tracking.

18 years) enrolled at *The Hospital for Sick Children* (Toronto, Canada) between January 2021 and December 2022. To validate the proposed inverse modeling framework, this work focuses on the healthy volunteer (HV) subset ($n = 20$). Included HVs had no history of cardiac disease and exhibited normal findings on standard transthoracic echocardiography.

Clinical variables

Standard demographics and anthropometrics, including age, sex, body mass index (BMI), and body surface area (BSA), were obtained for each subject (Table 2). Standard transthoracic echocardiography provided the geometric and volumetric indices required for the modelling workflow, specifically interventricular septal thickness at end-diastole (IVSd) and left-ventricular end-diastolic and end-systolic volumes (LVEDV and LVESV). These measurements were used to initialise the subject-specific geometry and to anchor model volumes during personalisation.

Derivation of target stiffness assessments

Each participant underwent a single imaging session at rest, recording 10 cardiac cycles. These multiple acquisitions were combined to generate one representative stiffness curve per subject. Since computational model outputs are generated in continuous physical time, they are subsequently mapped to this discrete phase grid for calibration (see Sec. 2.5.1). The resulting stiffness assessments (Fig. 3) illustrate the physiological inter-subject variability in diastolic baseline and systolic excursion, serving as the primary target data for model personalisation.

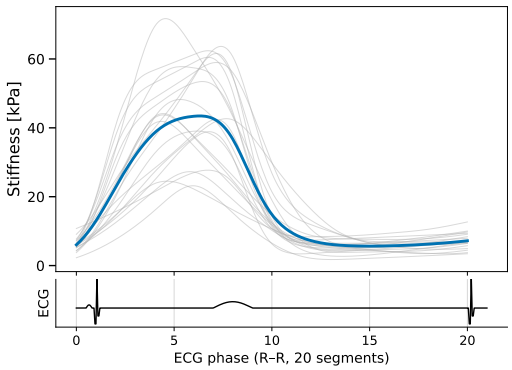


Fig. 3: Cycle-resolved myocardial stiffness variations of the cohort ($n = 20$). Thin gray lines represent individual subject acquisitions obtained over 20 ECG-gated phases, while the thick blue curve depicts the group average.

2.3 0D Model Formulation

We use a 0D-EM that captures global biventricular dynamics at a fraction of the cost of fully three-dimensional simulations (Caruel et al. 2013).

The model couples (i) a closed-loop lumped parameter circulation and (ii) a spherical biventricular mechanics model driven by an EM activation law (Fig. 4). The resulting system of ordinary differential equations (ODEs) is solved numerically; each simulation is run for seven cardiac cycles to reach a periodic hemodynamic regime, and only the final cycle is analysed.

Closed-loop lumped parameter circulation

The vascular system is represented using the electro-hydraulic analogy, a widely adopted approach in cardiovascular modeling, in which resistances (R) account for viscous losses and compliances (C) represent elastic storage (Westerhof et al. 2009; Liu et al. 2024). Systemic and pulmonary arteries are modeled with three-element Windkessel (RCR) compartments, while venous return is represented with two-element

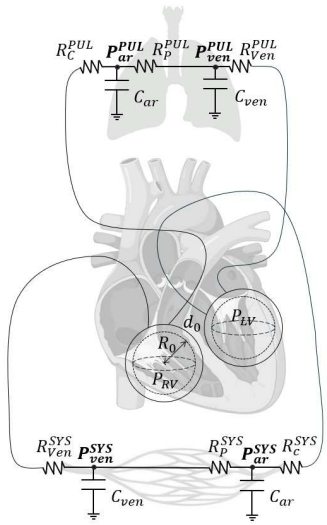


Fig. 4: Coupling between the biventricular mechanics and the closed-loop circulation model.

(RC) compartments, yielding a closed-loop configuration (Westerhof et al. 2009; Stergiopulos et al. 1992). This module provides the loading pressures acting on each ventricle: $P_{\mathrm{at}}(t)$, $P_{\mathrm{ar}}(t)$, and $P_{\mathrm{ve}}(t)$ and the corresponding flows, thereby accounting for preload and afterload effects. Full governing equations and parameter definitions are provided in Appendix A (Section A.5).

Biventricular mechanics under spherical reduction

Ventricular mechanics follow the BCS formulation (Bestel et al. 2001) in its energy-consistent extension (Chapelle et al. 2012), reduced to a 0D spherical setting as in Caruel et al. (2013).

Each ventricle is idealized as a thick-walled sphere (reference cavity radius R_0, wall thickness d_0), whose deformation is described by a single radial displacement $y(t)$. The resulting kinematics define the cavity volume $V(t)$ and the stretch measure $\lambda(t)$ used throughout the model. A full derivation of the spherical kinematics and governing relations is provided in Appendix A, Section A.2.

This reduced description preserves incompressibility and yields physiologically interpretable global outputs, including ventricular pressure $P(t)$ and cavity volume $V(t)$, which are used downstream for phase mapping and calibration.

2.3.1 Electromechanical activation

In the EM module, electrical activation drives calcium-dependent cross-bridge kinetics and generates an active stress state $\tau_c(t)$ and an associated active stiffness state $k_c(t)$. In the reduced moment formulation, k_c and τ_c correspond to the first moments of the attached cross-bridge distribution and evolve according to coupled ODEs together with the contractile strain e_c (Appendix A, Sections A.3 and A.4).

Activation timing is prescribed by the depolarized fraction $f_{\mathrm{depo}}(t) \in [0,1]$. We define the attachment and detachment rate contributions as

$$\begin{aligned} u^+(t) &= k_{\mathrm{ATP}}\, f_{\mathrm{depo}}(t), \\ u^-(t) &= k_{\mathrm{SR}}\big(1 - f_{\mathrm{depo}}(t)\big), \end{aligned} \tag{1}$$

and the resulting active control signal

$$u(t) = u^+(t) - w(t)\, u^-(t),$$

where $u(t)$ governs cross-bridge activation. k_{ATP} and k_{SR} set activation and relaxation kinetics, while $w(t) \in (0,1]$ accounts for load-dependent relaxation. The temporal evolution $u(t)$ and its relationship to the generated active stress $\tau_c(t)$ is illustrated in Figure 5 (Marchesseau et al. 2013). In the personalisation pipeline, active behaviour is controlled by the kinetic rates k_{ATP} and k_{SR} and by an amplitude parameter k_0 introduced in the active constitutive law (Eq. 29).

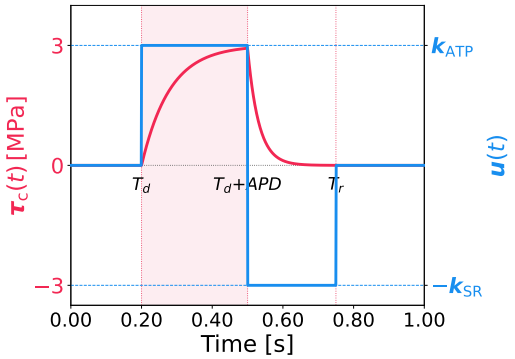


Fig. 5: Active stress $\tau_c(t)$ (pink) and control signal $u(t)$ (blue) over a cardiac cycle. The highlighted interval marks active generation from depolarisation onset (T_d) through APD to the end of relaxation (T_r).

2.4 Myocardial Stiffness Model

At the tissue level, myocardium is represented by a Hill-Maxwell rheological assembly (Fig. 6) comprising two parallel branches: an *active* contractile branch driven by cross-bridge kinetics, and a *passive-viscous* matrix branch accounting for hyperelasticity and dissipation. Under the spherical reduction, the resulting wall stress Σ_{sph} is given by the sum of the two branch contributions (Appendix A, Sec. A.3).

We model the measured MS as the superposition of a *passive* contribution derived from the incremental response of the hyperelastic matrix under the stretch $\lambda(t)$ and an *active* contribution, governed by the cross-bridge state variables:

$$k_{\text{model}}(t) = k_{\text{pass}}(t) + k_{\text{act}}(t). \tag{2}$$

The passive term provides the non-zero baseline observed in diastole, while the active term captures the systolic rise and subsequent relaxation. This decomposition enables sequential calibration, described in Section 2.5.

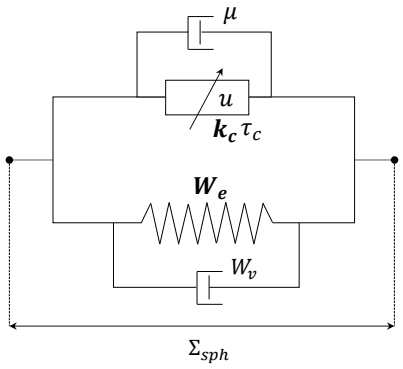


Fig. 6: Hill-Maxwell rheological representation adopted for the myocardial tissue. The model consists of two parallel branches: a passive branch (bottom) representing the hyperelastic matrix potential (W_e) and viscosity (W_v), and an active branch (top) describing cross-bridge contractility (u, k_c, τ_c) and damping (μ). Σ_{sph} represents the total resulting wall stress.

2.4.1 Passive hyperelastic baseline

The passive branch represents the nonlinear, nearly incompressible response of the myocardial matrix, whose strain-stiffening is associated with collagen recruitment and titin elongation.

We describe this behaviour within an isotropic incompressible hyperelastic framework, where the passive stress derives from a strain-energy density (SED) function W written in terms of the invariants of the right Cauchy-Green tensor $\mathbf{C} = \mathbf{F}^{\mathsf{T}}\mathbf{F}$, with $\mathbf{F}$ the deformation gradient (Holzapfel and Ogden 2009). We use the Mooney-Rivlin SED:

$$W(I_1, I_2) = C_1\,(I_1 - 3) + C_2\,(I_2 - 3), \tag{3}$$

where $I_1 = \operatorname{tr}(\mathbf{C})$ and $I_2 = \frac{1}{2}\big[(\operatorname{tr}\mathbf{C})^2 - \operatorname{tr}(\mathbf{C}^2)\big]$, and C_1, C_2 are material constants (units of stress). Incompressibility is enforced by a Lagrange multiplier p, yielding the standard stress forms

$$\begin{aligned}
\mathbf{S} &= -p\,\mathbf{C}^{-1} + 2\,\frac{\partial W}{\partial \mathbf{C}},\\
\boldsymbol{\sigma} &= \frac{2}{J}\,\mathbf{F}\,\frac{\partial W}{\partial \mathbf{C}}\,\mathbf{F}^{\mathsf{T}} - p\,\mathbf{I},\\
J &= \det \mathbf{F}.
\end{aligned}$$

To improve identifiability from the limited diastolic portion of the elastography data, we reduce the parameter space by imposing $C_1 = C_2$.

Spherical incompressible kinematics and volume-to-stretch mapping

To embed the hyperelastic law into the reduced 0D ventricle, we adopt a classical spherical idealisation with spatially uniform deformation (Caruel et al. 2013). In principal directions, we assume equibiaxial stretch, i.e. identical stretch in the two tangential directions, and incompressibility:

$$\lambda_\theta = \lambda_\phi = \lambda, \qquad \lambda_r = \lambda^{-2}, \tag{4}$$

It follows that $\mathbf{F} = \operatorname{diag}(\lambda, \lambda, \lambda^{-2})$ and $\mathbf{C} = \operatorname{diag}(\lambda^2, \lambda^2, \lambda^{-4})$, such that the invariants become:

$$I_1 = 2\lambda^2 + \lambda^{-4}, \qquad I_2 = 2\lambda^{-2} + \lambda^4. \tag{5}$$

The left ventricle (LV) is characterized by a single cavity radius $r(t)$, where $V(t) = \frac{4}{3}\pi r(t)^3$. Consequently, the tangential stretch scales with the cubic root of the volume ($r(t) \propto V(t)^{1/3}$). Using

the LV volume $V(t)$ predicted by the 0D model, we define the effective stretch trajectory:

$$\lambda(t) = \lambda_{\text{pre}} \left(\frac{V(t)}{V_{\text{ref}}} \right)^{1/3}, \tag{6}$$

where $\lambda_{\text{pre}} > 1$ denotes a physiological pre-stretch and V_{ref} is the reference volume.

In Eq. (6), the volume-to-stretch mapping requires a reference volume V_{ref} that anchors the kinematics. In the reduced biomechanical framework of Chapelle and Le Gall (2023), V_{ref} is associated with the passive zero-pressure equilibrium, considered to be the configuration of minimum passive potential energy. Because this state is not directly observable *in vivo*, it is typically inferred indirectly, for instance through an EDPVR-based normalization.

Here we adopt an *operational* reference tied to the ECG-gated SWE sampling. Let $x_{\min}$ denote the phase sample at which $k_{\text{SWE}}(x)$ is minimal on the 20-point SWE grid, and let $t(x)$ be the time-phase mapping of the last simulated cycle (defined in Section 2.5.1). We set

$$V_{\text{ref}} := V_{\text{model}}\big(t(x_{\min})\big).$$

This anchors the kinematic mapping to a reproducible low-tension phase supported by the data, enforces $\lambda\big(t(x_{\min})\big) = \lambda_{\text{pre}}$, and provides a physiologically meaningful normalization while remaining consistent with the spherical idealisation.

Incremental shear modulus, passive shape function, and calibration form

Since SWE probes a shear-like incremental response, we characterize the passive contribution through the incremental shear modulus $\mu_{\theta\phi}$ in the tangential plane (θ, ϕ) associated with the spherical stretch state (details in Appendix A). For a Mooney-Rivlin material under principal stretches,

$$\mu_{\theta\phi}(\lambda) = 2\Big(C_1\,\lambda^2 + C_2\,\lambda^{-2}\Big), \tag{7}$$

which recovers the small-strain limit $\mu_0 = \mu_{\theta\phi}(1) = 2(C_1 + C_2)$. To reduce parameter indeterminacy, we apply the constraint $C_1 = C_2$ and introduce a single stiffness scale $c := \mu_0$ (units of stress). This implies $C_1 = C_2 = c/4$, simplifying the modulus to:

$$\begin{aligned} \mu_{\theta\phi}(\lambda) &= c\,\phi(\lambda), \\ \phi(\lambda) &= \frac{\lambda^2 + \lambda^{-2}}{2}, \quad \text{with } \phi(1) = 1. \end{aligned} \tag{8}$$

Physically, the term λ^2 reflects the increase in tangential tension with stretch, while λ^{-2} captures the transverse compression induced by incompressibility in the spherical shell. Finally, the passive contribution to the measured stiffness is modeled as an affine function of this shape factor:

$$k_{\text{pass}}(t) = c\,\phi\big(\lambda(t)\big) + b, \tag{9}$$

where $c > 0$ sets the small-strain passive stiffness scale and b is an optional offset accounting for residual baseline mismatch.

2.4.2 Active stiffness contribution

Active behaviour is parameterised by three quantities: the stiffness amplitude k_0 [kPa], the cross-bridge attachment rate k_{ATP} [s^{-1}], and the detachment rate k_{SR} [s^{-1}]. These parameters govern the dynamics of the cross-bridge moment states (e_c, k_c, τ_c) via the activation rates in Eq. (1). Within this reduced moment-closure formulation, sarcomere-scale cross-bridge kinetics are upscaled into a macroscopic active stress $\tau_c(t)$ and an associated active stiffness $k_c(t)$. The full ODE system coupling e_c, k_c, τ_c is reported in Appendix A Sec. A.4. In practice, the model active stiffness contribution is defined as

$$k_{\text{act}}(t) \equiv k_c(t). \tag{10}$$

2.5 Parameter Calibration

Figure 1 summarises the sequential calibration workflow: (i) phase mapping of SWE and model outputs onto a common normalised axis, (ii) late-diastolic identification of the passive component, and (iii) CMA-ES estimation of active parameters followed by reconstruction of total stiffness.

Clinical SWE provides one stiffness curve per subject sampled at 20 ECG-gated phases $\{x_i\}_{i=1}^{20}$ over one R–R interval. The 0D model is integrated in physical time; its last simulated cycle is mapped to the same normalised phase axis and

compared to SWE on the 20-point grid. Working on the phase axis, total stiffness follows the active–passive decomposition (Eq. (2)),

$$k_{\text{model}}(x) = k_{\text{act}}(x;\boldsymbol{\theta}) + k_{\text{pass}}(x;c,b), \tag{11}$$

with $\boldsymbol{\theta} = (k_0, k_{\text{ATP}}, k_{\text{SR}})$ and $k_{\text{pass}}(x;c,b) = c\,\phi\big(\lambda(x)\big) + b$. Calibration is sequential: we first identify (c,b) on late diastole, then identify $\boldsymbol{\theta}$ from the residual active target.

2.5.1 Phase normalisation and sampling

Clinical SWE is provided at 20 ECG-gated frames $s_i = 1,\dots,20$. We represent these samples on a normalised phase axis $x \in [0,1)$ via

$$x_i = \frac{s_i - 1}{20}, \qquad i = 1,\dots,20,$$

and denote the corresponding measurements by $k_{\text{SWE}}(x_i)$. To compare the model against data, the 0D system is simulated to a periodic steady state (typically seven cycles). The final cycle $t \in [t_0, t_0 + T]$ is extracted and mapped to phase by:

$$t(x) = t_0 + xT, \qquad x \in [0,1). \tag{12}$$

Any model output $q(t)$ is then defined in phase form as $q(x) := q(t(x))$. Note that the domain is half-open to enforce periodicity without duplicating the endpoint. The phase-mapped model stiffness $k_{\text{model}}(x)$ is interpolated at the clinical sampling points $\{x_i\}$, ensuring a one-to-one comparison between $k_{\text{model}}(x_i)$ and $k_{\text{SWE}}(x_i)$. We define the minimum-stiffness SWE index, along with its associated phase and time, as:

$$\begin{aligned} i_{\min} &= \arg\min_{i\in\{1,\dots,20\}} k_{\text{SWE}}(x_i), \\ x_{\min} &= x_{i_{\min}} \in [0,1), \\ t_{\min} &= t(x_{\min}) = t_0 + x_{\min} T. \end{aligned} \tag{13}$$

Finally, end-diastole is defined as the last ECG-gated sample on this grid:

$$i_{\text{ED}} = 20, \qquad x_{\text{ED}} = x_{20} = \frac{19}{20}.$$

2.5.2 Passive parameter identification

Passive parameters are identified on a late-diastolic window W_{dia} where active tone is assumed negligible. On the 20-point phase grid, W_{dia} is defined as the consecutive set of SWE samples from the minimum-stiffness index $i_{\min}$ to end-diastole i_{ED}:

$$W_{\text{dia}} = \{i_{\min}, i_{\min}+1, \dots, i_{\text{ED}}\}.$$

Stretch is computed from the simulated LV volume trace using the spherical mapping in Eq. (6). We anchor the kinematics at the minimum-stiffness phase by defining the operational reference volume as: $V_{\text{ref}} := V_{\text{model}}(x_{\min})$. This enforces $\lambda(x_{\min}) = \lambda_{\text{pre}}$ by construction (see also Section 2.4.1). The passive prediction at the SWE samples is given by $k_{\text{pass}}(x_i;c,b) = c\,\phi\big(\lambda(x_i)\big) + b$. We estimate the passive parameters $(\hat{c},\hat{b})$ via weighted least squares:

$$(\hat{c},\hat{b}) = \arg\min_{c\ge 0,\, b\ge 0} \sum_{i\in W_{\text{dia}}} w_i \Big(k_{\text{SWE}}(x_i) - c\,\phi\big(\lambda(x_i)\big) - b\Big)^2. \tag{14}$$

with weights w_i chosen to increase toward x_{ED}, to anchor the fit at end-diastole. In the primary pipeline, we set $b = 0$ to reduce parameter coupling; the offset b is free only if a persistent baseline mismatch remains after phase mapping.

Finally, subtracting the fitted passive component yields the active target samples used for active calibration:

$$k_{\text{act,target}}(x_i) = k_{\text{SWE}}(x_i) - k_{\text{pass}}(x_i;\hat{c},\hat{b}), \quad i \in \{1,\dots,20\}. \tag{15}$$

2.5.3 Active parameter identification with CMA-ES

Active parameters $\boldsymbol{\theta} = (k_0, k_{\text{ATP}}, k_{\text{SR}})$ are estimated by minimizing the MAP cost function:

$$\hat{\boldsymbol{\theta}} = \arg\min_{\boldsymbol{\theta}\in\Theta} \mathcal{J}_{\text{data}}(\boldsymbol{\theta}) + \lambda_{\text{prior}}\,\mathcal{J}_{\text{prior}}(\boldsymbol{\theta}), \tag{16}$$

where $\lambda_{\text{prior}} \ge 0$ weights the regularization against data fidelity. The search space Θ is constrained by

Table 1: Active parameter search space.

Parameter	Bounds	Unit
Stiffness scale (k_0)	$[10, 100]$	kPa
ATP rate (k_{ATP})	$[2.0, 30.0]$	s^{-1}
Return rate (k_{SR})	$[2.0, 30.0]$	s^{-1}

physiologically plausible bounds (Table 1), derived from literature (Banus et al. 2021; Marchesseau et al. 2013) to prevent non-physical solutions.

The data term $\mathcal{J}_{\mathrm{data}}$ measures the discrepancy between the simulated active contribution and the active target. To incorporate population-level knowledge into the individual personalization process, the regularization term $\mathcal{J}_{\mathrm{prior}}$ uses a log-Gaussian prior:

$$\mathcal{J}_{\mathrm{prior}}(\boldsymbol{\theta}) = \tfrac{1}{2}\big(\log\boldsymbol{\theta} - \boldsymbol{\mu}\big)^{\top}\boldsymbol{\Sigma}^{-1}\big(\log\boldsymbol{\theta} - \boldsymbol{\mu}\big), \quad (17)$$

where $\boldsymbol{\mu} \in \mathbb{R}^3$ and $\boldsymbol{\Sigma} \in \mathbb{R}^{3\times 3}$ are the cohort mean and covariance matrix of $\log\boldsymbol{\theta}$, respectively.

The covariance $\boldsymbol{\Sigma}$ quantifies expected inter-subject variability of the active parameters: smaller variances enforce tighter regularization toward the cohort average, whereas larger variances allow broader subject-specific deviations. These statistics are estimated once at the cohort level and then kept fixed during subject personalization. Thus, the prior promotes physiological consistency at the population level, while the MAP optimization (Eq. (16)) remains patient-specific by balancing the prior against the individual data misfit $\mathcal{J}_{\mathrm{data}}$.

Optimization is performed using the CMA-ES algorithm (Hansen 2007, 2023) with a population size of $\lambda_{\mathrm{CMA}} = 16$ and a maximum of 30 iterations. To ensure robustness against stochastic initialization, we performed 10 independent runs, allowing for up to 3 internal random restarts if stagnation is detected (stagnation limit: 8 generations). The entire calibration procedure takes approximately 15 minutes per subject (wall-clock time on a standard multi-core workstation), exploring a total computational budget of ∼4,800 model evaluations.

Objective function

The data term $\mathcal{J}_{\mathrm{data}}$ is a composite misfit combining amplitude error, shape agreement, and peak timing. It compares the simulated active contribution $\{k_{\mathrm{act}}(x_i;\boldsymbol{\theta})\}$ against the target $\{k_{\mathrm{act,target}}(x_i)\}$:

$$\begin{aligned}\mathcal{J}_{\mathrm{data}}(\boldsymbol{\theta}) = w_{\mathrm{nMAE}}\,\mathrm{nMAE}\Big(k_{\mathrm{act}}, k_{\mathrm{target}}\Big) \\ + w_{\rho}\Big(1 - \rho(k_{\mathrm{act}}, k_{\mathrm{target}})\Big) \\ + w_{\mathrm{peak}}\,\Delta x_{\mathrm{peak}}^2.\end{aligned} \quad (18)$$

Here, ρ is the Pearson correlation coefficient and Δx_{peak} is the phase difference between peak locations. The term nMAE denotes the mean absolute error normalized by the interquartile range of the target signal (see Appendix B). The weights were empirically tuned to balance amplitude and phase accuracy and are fixed across all subjects as $w_{\mathrm{MAE}} = 1.2$, $w_{\rho} = 0.1$, and $w_{\mathrm{peak}} = 0.8$.

Reconstruction

The final reconstructed stiffness on the phase axis is obtained by summing the calibrated components,

$$k_{\mathrm{model}}(x) = k_{\mathrm{pass}}(x;\hat{c},\hat{b}) + k_{\mathrm{act}}(x;\hat{\boldsymbol{\theta}}), \quad (19)$$

which can be mapped back to the physical time domain t via Eq. (12).

3 Results

We first report cohort characteristics and the measured stiffness profiles, followed by the model calibration performance, parameter estimates, and the resulting active-passive decomposition.

3.1 Cohort summary

Demographics and echocardiographic indices are summarised in Table 2. The cohort comprised 11 female and 9 male HVs with median age of 10.49 years [6.87, 14.63] and heart rate of 73.0 bpm [68.75, 93.25]. Subjects exhibited normal geometry and systolic function, characterised by an IVSd of 0.58 cm [0.51, 0.72], LV dimensions within the normal range (Z-scores < 2), LVEF of 62.5% [59.75, 64.25], and GLS of −21% [−21, −20]. Cycle-resolved SWE stiffness profiles (Fig. 3) demonstrated a consistent pattern: a systolic stiffness rise followed by diastolic relaxation. The curves were characterised by a late-diastolic baseline of 6.49 [4.65, 7.16] kPa and a systolic peak of 46.38 [38.83, 59.03] kPa occurring at normalized time $t_n = 0.28$ [0.24, 0.31].

Table 2: HV ($n = 20$) characteristics. Values are median [Q1, Q3]. BSA: Body Surface Area; LVEDVi/LVESVi: End-diastolic/systolic volumes indexed to BSA.

Demographics	
Sex [Female/Male]	11/9
Age [years]	10.49 [6.87, 14.63]
BMI [kg/m^2]	18.46 [15.11, 21.69]
BSA [m^2]	1.25 [0.78, 1.70]
Heart Rate [bpm]	73.0 [68.75, 93.25]
Conventional Echography	
IVSd [cm]	0.58 [0.51, 0.72]
LVEDV [mL]	60.50 [40.25, 68.50]
LVEDVi [mL/m^2]	47.68 [40.30, 50.60]
LVESV [mL]	21.00 [14.75, 27.00]
LVESVi [mL/m^2]	18.64 [14.40, 19.94]
LVEF [%]	62.50 [59.75, 64.25]
GLS [%]	−21 [−21, −20]

3.2 Model calibration results

3.2.1 Parameter estimates and variability

The calibration pipeline converged for all 20 volunteers. Agreement between simulated and measured trajectories was quantified by the zero-lag cross-correlation coefficient r_{xcorr} (median $r_{\text{xcorr}} =$ 0.997 [0.991, -0.998]). The calibration yielded subject-specific estimates of the passive scaling factor $\hat{c}$, the contractility amplitude $\hat{k}_0$, and the activation/relaxation kinetic rates $\hat{k}_{\text{ATP}}$ and $\hat{k}_{\text{SR}}$ (Table 3), within physiologically plausible ranges for normal myocardium (Banus et al. 2021; Marchesseau et al. 2013).

The passive scaling $\hat{c}$ was identified over the late-diastolic window using weighted least squares. Active parameters were estimated with CMA-ES; robustness was assessed by repeating the optimisation from multiple random seeds (Molléro et al. 2018). For each subject, dispersion in the final objective value was summarised by $J_{\text{med}}/J_{\text{min}}$, which was close to 1 (median 1.05 [1.02, 1.09]; Fig. 7a), indicating consistent convergence to the same minimum.

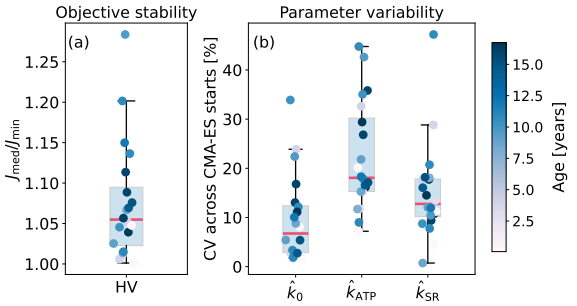


Fig. 7: Robustness and variability in HV ($n = 20$). (a) Objective function stability across random CMA-ES initialisations ($J_{\text{med}}/J_{\text{min}}$), with J the final cost. Ratios near 1 indicate convergence to the same minimum. (b) Across-start parameter variability (CV, %); dots denote subjects (color = age) and boxplots show median and IQR.

To quantify the stability of parameter estimates, we calculated the within-subject coefficient of variation (CV), defined as the ratio of the standard deviation to the mean across initializations: $CV = (\sigma/\mu) \times 100\%$. This yielded median CVs of 6.7% for $\hat{k}_0$, 18.1% for $\hat{k}_{\text{ATP}}$, and 12.8% for $\hat{k}_{\text{SR}}$ (Fig. 7b). CV($\hat{k}_0$) and CV($\hat{k}_{\text{ATP}}$) were correlated (Pearson $\rho = 0.77$), whereas no clear association with age was observed. Importantly, our goal was not to enforce identical parameter values across subjects, as genuine age-related physiological heterogeneity is expected.

3.2.2 Waveform fidelity and active-passive decomposition

Goodness-of-fit metrics are reported in Table 3, including the zero-lag cross-correlation r_{xcorr} (median 0.997) and the normalized root mean square error nRMSE (median 1.02). Figure 8 shows cohort-level waveforms of the measured stiffness $k_{\text{SWE}}(x)$ and the calibrated prediction $k_{\text{model}}(x)$, together with the active-passive decomposition of $k_{\text{model}}(x)$ into $k_{\text{act}}(x)$ and $k_{\text{pass}}(x)$. Representative subject-level decompositions are shown in Fig. 9.

4 Discussion

This work presents a waveform-based inverse modeling framework that links cycle-resolved SWE

Table 3: Calibrated parameters and waveform fit metrics. Values are median [Q1, Q3]

Calibrated Parameters	**Estimate**
$\hat{c}$ [kPa]	9.76 [1.02, 23.4]
$\hat{k}_0$ [kPa]	49.1 [36.7, 55.1]
$\hat{k}_{\mathrm{ATP}}$ [s^{-1}]	11.1 [6.61, 17.0]
$\hat{k}_{\mathrm{SR}}$ [s^{-1}]	13.2 [11.5, 24.7]
Waveform Fit Metrics	
nRMSE [-]	1.02 [0.80, 1.35]
r_{xcorr} [-]	0.997 [0.991, 0.998]

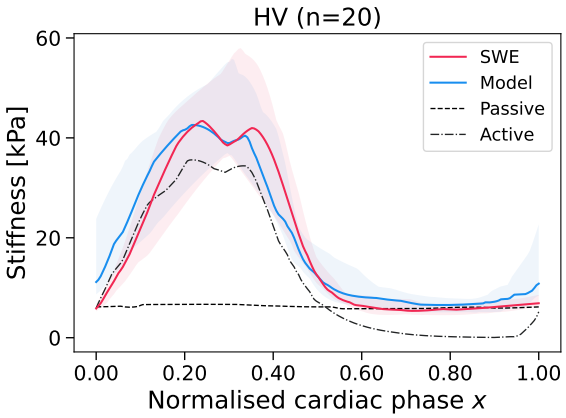
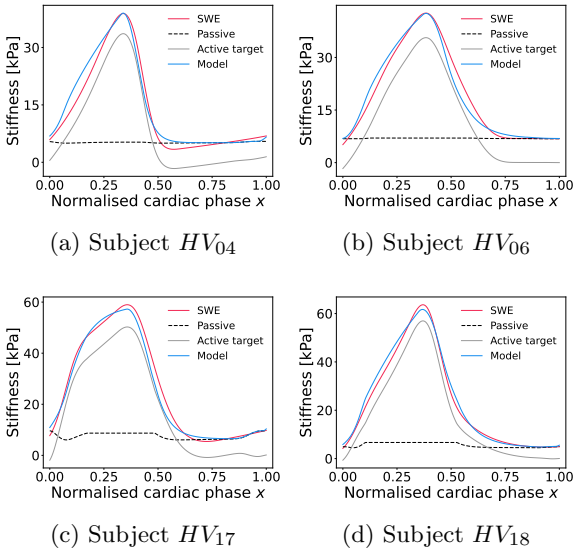


Fig. 8: Cohort-level SWE stiffness and calibrated model fits over normalised phase $x \in [0, 1]$. Solid lines show medians and shaded bands IQRs for $k_{\mathrm{SWE}}(x)$ and $k_{\mathrm{model}}(x)$; the model median is also decomposed into passive and active components.



(a) Subject HV_{04} (b) Subject HV_{06}

(c) Subject HV_{17} (d) Subject HV_{18}

Fig. 9: Representative subject-level stiffness decompositions. Measured clinical stiffness (k_{SWE}) is compared with the calibrated model fit (k_{model}), which is further decomposed into passive and active contributions.

stiffness measurements to subject-specific parameters of a closed-loop 0D-EM heart model. Our central methodological contribution is a sequential active-passive decomposition.

We first identify a passive baseline in late diastole using a hyperelastic-derived stretch shape function. We then estimate the maximum active stiffness k_0 and the cross-bridge rates (k_{ATP}, k_{SR}) from the residual active target via Bayesian MAP optimization using CMA-ES.

Unlike approaches that reduce SWE to a few scalar descriptors (e.g., peak or mean stiffness), our objective function enforces agreement at the waveform level. We employ a composite objective function combining amplitude error, shape correlation, and peak-timing mismatch on the ECG-gated phase grid. This leverages information distributed across the entire cardiac cycle, rather than relying on isolated time points.

A critical ambiguity in stiffness interpretation lies in distinguishing passive remodeling from residual active tone. By anchoring the passive estimate in a late-diastolic period where active contribution is assumed negligible, we reduce coupling between the baseline level and active kinetics. This limits the risk of the optimizer compensating for elevated diastolic stiffness by inflating active parameters. The close agreement observed in healthy volunteers supports this separation: consistent with the theoretical framework of Caruel et al. (2013), the systolic stiffness rise is treated as a product of active mechanisms, while the passive component sets the diastolic baseline.

Convergence remained robust across random initializations, characterized by objective ratios near one and moderate within-subject variability for active parameters. Notably, this indicates the inverse problem is identifiable despite the sparse sampling of the SWE waveform.

Several assumptions should be considered when interpreting the estimated parameters.

The spherical reduction and isotropic constitutive choice neglect myocardial anisotropy and regional heterogeneity, which may affect the absolute physiological meaning of parameters even if subject-level fitting remains accurate. The present approach provides a consistent model-based mapping, but sensitivity to acquisition settings and wave-propagation effects warrants further study.

Finally, phase normalisation facilitates optimisation and inter-subject comparison but may attenuate timing differences; incorporating personalised electromechanical timing could further refine kinetic estimates.

5 Conclusion

We have developed and validated a physics-based computational framework that converts cycle-resolved SWE into subject-specific mechanical models. By solving the inverse problem through a sequential active-passive decomposition, the method resolves the indeterminacy often found in analyzing raw myocardial stiffness assessments. Application to healthy volunteers demonstrated parameter stability and adequate waveform agreement, suggesting that reduced-order electromechanical formulations can reproduce the primary dynamics of myocardial stiffness. This framework contributes to the development of SWE-informed digital twinning, offering a potential non-invasive means to characterize distinct mechanical pathways of cardiac remodeling in future clinical investigations.

Acknowledgements. This work has received funding from the French government through the National Research Agency (ANR) under the *PEPR Digital Health ChroniCardio* (22-PESN-0015), *3IA Côte d'Azur* and *IA Cluster* (ANR-19-3IA-0002 and ANR-23-IACL-0001), and *IHU Liryc* (ANR-10-IAHU-04). Additional support was provided by France 2030 and the European Union (Next Generation EU) through the *MediTwin* project. This work was also supported by the European Research Council (ERC) under the European Union's Horizon Europe research and innovation program (5D ULTRAFAST HCM project, grant agreement 101220327). We acknowledge the OPAL infrastructure (Université Côte d'Azur) for providing computational resources and technical support.

We also thank Giuseppe Orlando and Nicolas Drettakis for their support and helpful discussions.

Competing Interests. The authors have no competing interests to declare that are relevant to the content of this article.

Authors Contribution. CF: Conceptualization, methodology, software, data analysis, and original draft. MS: Supervision, study design, and critical revision. MV and OV: Clinical resources, data acquisition protocol, and medical interpretation. All authors reviewed and approved the final manuscript.

References

Banus J, Lorenzi M, Camara O, et al (2021) Biophysics-based statistical learning: Application to heart and brain interactions. Medical Image Analysis 72. https://doi.org/10.1016/j.media.2021.102089

Bestel J, Clément F, Sorine M (2001) A biomechanical model of muscle contraction. In: Medical Image Computing and Computer-Assisted Intervention (MICCAI), pp 1159–1161

Caenen A, Bézy S, Pernot M, et al (2024) Ultrasound shear wave elastography in cardiology. JACC: Cardiovascular Imaging 17(3):314–329. https://doi.org/10.1016/j.jcmg.2023.12.007

Caruel M, Chabiniok R, Moireau P, et al (2013) Dimensional reductions of a cardiac model for effective validation and calibration. Biomechanics and Modeling in Mechanobiology 12(4):815–829. https://doi.org/10.1007/s10237-012-0446-5

Chabiniok R, Wang VY, Hadjicharalambous M, et al (2016) Multiphysics and multiscale modelling, data–model fusion and integration of organ physiology in the clinic: ventricular cardiac mechanics. Interface Focus 6(2):20150083. https://doi.org/10.1098/rsfs.2015.0083

Chapelle D, Le Gall A (2023) A biomechanics-based parametrized cardiac end-diastolic pressure–volume relationship for accurate patient-specific calibration and estimation. Scientific Reports 13:9. https://doi.org/10.1038/s41598-023-38196-5

Chapelle D, Le Tallec P, Moireau P, et al (2012) An energy-preserving muscle tissue model: Formulation and compatible discretizations. International Journal for Multiscale Computational Engineering 10(2):189–211. https://doi.org/10.1615/IntJMultCompEng.2011002360

Cikes M, Tong L, Sutherland GR, et al (2014) Ultrafast cardiac ultrasound imaging: Technical principles, applications, and clinical benefits. JACC: Cardiovascular Imaging 7(8):812–823. https://doi.org/10.1016/j.jcmg.2014.06.004

Ferrario C, Padilla JR, Venet M, et al (2025) Myocardial stiffness quantification using ultrasound shear wave elastography and reduced modeling for subject-specific simulations. In: Chabiniok R, Zou Q, Hussain T, et al (eds) Functional Imaging and Modeling of the Heart (FIMH 2025), pp 53–64, https://doi.org/10.1007/978-3-031-94562-5_5

Guccione JM, Waldman LK, McCulloch AD (1993) Mechanics of active contraction in cardiac muscle: Part ii—cylindrical models of the systolic left ventricle. Journal of Biomechanical Engineering 115(1):82–90. https://doi.org/10.1115/1.2895474

Hansen N (2007) The cma evolution strategy: A comparing review. In: Towards a New Evolutionary Computation, Studies in Fuzziness and Soft Computing, vol 192. Springer, p 75–102, https://doi.org/10.1007/3-540-32494-1_4

Hansen N (2023) The cma evolution strategy: A tutorial. URL https://arxiv.org/abs/1604.00772, arXiv:1604.00772

Holzapfel GA, Ogden RW (2009) Constitutive modelling of passive myocardium: a structurally based framework for material characterization. Philosophical Transactions of the Royal Society A: Mathematical, Physical and Engineering Sciences 367(1902):3445–3475. https://doi.org/10.1098/rsta.2009.0091

Liu X, Mo C, Li J, et al (2024) Development of a lumped parameter model of human whole body circulatory loop. IEEE Access https://doi.org/10.1109/ACCESS.2024.3491112, early access article

Malik A, Villalobos Lizardi JC, Baranger J, et al (2024) Comparison between acoustic radiation force-induced and natural wave velocities for myocardial stiffness assessment in hypertrophic cardiomyopathy. JACC: Cardiovascular Imaging 17(2):223–225. https://doi.org/10.1016/j.jcmg.2023.07.015

Marchesseau S, Delingette H, Sermesant M, et al (2013) Preliminary specificity study of the bestel–clément–sorine electromechanical model of the heart using parameter calibration from medical images. Journal of the Mechanical Behavior of Biomedical Materials 20:259–271. https://doi.org/10.1016/j.jmbbm.2012.11.021

Molléro R, Pennec X, Delingette H, et al (2018) Population-based priors in cardiac model personalization for consistent parameter estimation in heterogeneous databases. Computer Methods in Applied Mechanics and Engineering 384:113931. https://doi.org/10.1002/cnm.3158

Muslov SA, Vasyuk YA, Zavialova AI, et al (2023) Mathematical modeling of biomechanical elastic and hyperelastic properties of the myocardium. Medical Academic Journal 23(4):53–68. https://doi.org/10.17816/MAJ624108

Pernot M, Couade M, Mateo P, et al (2011) Real-time assessment of myocardial contractility using shear wave imaging. JACC 58(1):65–72. https://doi.org/10.1016/j.jacc.2011.02.042

Sagawa K, Suga H, Shoukas AA, et al (1977) End-systolic pressure/volume ratio: A new index of ventricular contractility. The American Journal of Cardiology 40:748–753. https://doi.org/10.1016/0002-9149(77)90192-8

Sermesant M, Chabiniok R, Chinchapatnam P, et al (2011) Patient-specific electromechanical models of the heart for the prediction of pacing acute effects in crt: A preliminary clinical validation. Medical Image Analysis 15(3):437–448. https://doi.org/10.1016/j.media.2011.07.003

Stergiopulos N, Young DF, Rowe TR (1992) Computer simulation of arterial flow with applications to arterial and aortic stenoses. Journal of Biomechanics 25(12):1477–1488. https://doi.org/10.1016/0021-9290(92)90060-E

Venet M, Baranger J, Malik A, et al (2025) Towards non-invasive assessment of myocardial work using myocardial stiffness and strain: a human pilot study. European Heart Journal - Cardiovascular Imaging 26(6):1051–1064. https://doi.org/10.1093/ehjci/jeaf089, published online May 30, 2025

Villalobos Lizardi JC, Baranger J, Nguyen MB, et al (2022) A guide for assessment of myocardial stiffness in health and disease. Nature Cardiovascular Research 1(1):8–22. https://doi.org/10.1038/s44161-021-00007-3

Villaverde AF, Tsiantis N, Banga JR (2019) Full observability and estimation of unknown inputs, states and parameters of nonlinear biological models. Journal of the Royal Society Interface 16(20190043). https://doi.org/10.1098/rsif.2019.0043

Villemain O, Correia M, Mousseaux E, et al (2019) Myocardial stiffness evaluation using noninvasive shear wave imaging in healthy and hypertrophic cardiomyopathic adults. JACC Cardiovasc Imaging 12(7 Pt 1):1135–1145. https://doi.org/10.1016/j.jcmg.2018.02.002

Villemain O, Baranger J, Friedberg MK, et al (2020) Ultrafast ultrasound imaging in pediatric and adult cardiology: Techniques, applications, and perspectives. JACC Cardiovasc Imaging 13(8):1771–1791. https://doi.org/10.1016/j.jcmg.2019.09.019

Westerhof N, Lankhaar JW, Westerhof BE (2009) The arterial windkessel. Medical & Biological Engineering & Computing 47:131–141. https://doi.org/10.1007/s11517-008-0359-2

A Full 0D-EM closed-loop model

A.1 Model overview and state variables

The model couples both the LV and RV to the systemic and pulmonary circulations through mechanical and active subsystems defined for each ventricle. Dynamics are governed by coupled ODEs. Table 4 summarizes the key model parameters. Unless stated otherwise, parameters are shared between ventricles. The state vector comprises:

- **Mechanical:** Radial displacement $y(t)$ and velocity $\dot{y}(t)$.
- **Contractile:** Contractile strain $e_c(t)$, active stiffness $k_c(t)$, and active stress variable $\tau_c(t)$. If load-dependent relaxation is active, the relaxation variable $w(t)$ is included.
- **Hemodynamic:** Ventricular pressure $P(t)$ and arterial pressure $P_{\mathrm{ar}}(t)$. Atrial pressure P_{at} and venous pressure P_{ve} are typically fixed boundary conditions or evolved via simple compliance.

The system is integrated forward from initial conditions until a periodic steady state is reached.

A.2 Spherical kinematics

The ventricle is modeled as a thick spherical shell of reference radius R_0 and wall thickness d_0. The radial mechanics are defined by the circumferential stretch $\lambda(t) = 1 + y(t)/R_0$. Under tissue incompressibility ($\det \mathbf{F} = 1$), the cavity volume and outflow are:

$$\begin{aligned} V(t) &= \tfrac{4\pi}{3} R_0^3 \, \lambda(t)^3, \\ Q(t) &= -\dot{V}(t) = -4\pi R_0^2 \, \lambda(t)^2 \, \dot{y}(t). \end{aligned} \tag{20}$$

A.3 Wall mechanics

The mechanical subsystem follows an energy-consistent rheological framework (Chapelle et al. 2012), consisting of an active element and Z-disk spring in series, positioned in parallel with a passive-viscous matrix. This is reduced to a 0D spherically symmetric model (Caruel et al. 2013) where stress equilibrium is governed by a single radial degree of freedom $y(t)$. The total spherical wall stress Σ_{sph} balances the cavity pressure and is the sum of active (σ_{1D}), passive (σ_{pass}), and viscous (σ_{visc}) components:

$$\Sigma_{\mathrm{sph}}(t) = \sigma_{1D}(t) + \sigma_{\mathrm{pass}}(t) + \sigma_{\mathrm{visc}}(t). \tag{21}$$

Here, σ_{1D} represents the fiber-direction active stress, while σ_{pass} and σ_{visc} account for the parallel hyperelastic and viscoelastic effects, respectively.

Passive and viscous stress

Deriving from a Mooney-Rivlin energy density and a dissipative pseudo-potential, the passive and viscous scalar stresses are (Caruel et al. 2013):

$$\sigma_{\mathrm{pass}} = 4(1 - \lambda^{-6})(C_1 + C_2\lambda^2), \tag{22}$$

$$\sigma_{\mathrm{visc}} = 8\mu(1 + \lambda^{-12})\lambda\,\dot{\lambda}, \tag{23}$$

where C_1, C_2 are stiffness moduli and μ is the wall viscosity.

Active stress

The active element acts in series with a Z-disk spring (E_s) to generate the spherical stress:

$$\sigma_{1D} = \frac{1+2e_c}{1+2e_{1D}}\left(\tau_c + \mu_c \dot{e}_c\right), \tag{24}$$

where $e_{1D} = (\lambda^2 - 1)/2$ is the macroscopic strain. The internal contractile strain e_c evolves via the series force balance:

$$\tau_c + \mu_c \dot{e}_c = E_s \frac{(e_{1D} - e_c)(1+2e_{1D})}{(1+2e_c)^3}. \tag{25}$$

Equation of motion

Radial momentum balance yields the governing ODE for $y(t)$:

$$\rho\, d_0\, \ddot{y} = P\,\lambda^2 - \frac{d_0}{R_0}\lambda\,\Sigma_{\text{sph}}, \tag{26}$$

where ρ is myocardial density and P is the ventricular pressure provided by the circulation model.

A.4 Cross-bridge dynamics

The active state is described by the density of attached cross-bridges $n(s,t)$ with normalized extension s. Following Chapelle et al. (2012), the macroscopic *active stiffness* k_c and *active stress* τ_c are defined as the first two moments of this distribution:

$$k_c(t) = k_0 \int_{\mathbb{R}} n(s,t)\, ds, \tag{27}$$

$$\tau_c(t) = k_0 \int_{\mathbb{R}} (s+s_0)\, n(s,t)\, ds, \tag{28}$$

where k_0 is the single-bridge stiffness scale and s_0 is a pre-strain parameter. The time evolution of these moments is governed by the attachment rate $u^+(t)$ and detachment rate $u^-(t)$, defined consistently with Eq. (1) in the main text:

$$u^+(t) = k_{\text{ATP}} f_{\text{depo}}(t), \quad u^-(t) = k_{\text{SR}}\big(1 - f_{\text{depo}}(t)\big).$$

The resulting ODEs for the active variables are:

$$\begin{aligned} \dot{k}_c &= -\Phi\, k_c + n_0(e_c)\, k_0\, u^+, \\ \dot{\tau}_c &= -\Phi\, \tau_c + n_0(e_c)\, \sigma_0\, u^+ + k_c \dot{e}_c. \end{aligned} \tag{29}$$

Here, the destruction rate is $\Phi(t) = u^+ + w(t)u^- + \alpha|\dot{e}_c|$, which accounts for turnover and velocity-dependent bridge disruption. The source term scale is defined as $\sigma_0 = k_0(s_0 + 1/2)$. If load-dependent relaxation is enabled, $w(t)$ evolves according to:

$$\alpha_r \dot{w} = m_0(e_c) - w, \tag{30}$$

where $m_0(e_c)$ is a decreasing function of contractile strain e_c. Otherwise, $w(t) \equiv 1$.

A.5 Circulatory coupling

Each ventricle is coupled to the circulation via a pressure-driven valve system and a *Windkessel* arterial load.

Valve law

Ventricular flow $Q(t)$ follows a piecewise-linear conductance law maintaining continuity across transitions:

$$Q(t) = \begin{cases} K_{\text{at}}\big(P - P_{\text{at}}\big), & P \le P_{\text{at}}, \\ K_{\text{iso}}\big(P - P_{\text{at}}\big), & P_{\text{at}} < P < P_{\text{ar}}, \\ K_{\text{ar}}\big(P - P_{\text{ar}}\big) + K_{\text{iso}}\big(P_{\text{ar}} - P_{\text{at}}\big) & P \ge P_{\text{ar}}. \end{cases} \tag{31}$$

where K_{at} and K_{ar} are filling and ejection conductances, and K_{iso} is a small leakage term for numerical stability. When $P \le P_{\text{at}}$, the atrioventricular valve opens (filling phase). In the intermediate range $P_{\text{at}} < P < P_{\text{ar}}$, both valves are effectively closed (isovolumic phase), though a small leakage K_{iso} is permitted. Finally, when $P \ge P_{\text{ar}}$, the aortic valve opens (ejection).

Arterial afterload

The arterial pressure P_{ar} is governed by a three-element (RCR) Windkessel model:

$$R_p C_{\text{ar}} \dot{P}_{\text{ar}} + (P_{\text{ar}} - P_{\text{ve}}) = (R_p + Z_c)\, Q + R_p Z_c C_{\text{ar}}\, \dot{Q}. \tag{32}$$

parameterized by proximal characteristic impedance Z_c, arterial compliance C_{ar}, peripheral resistance R_p, and downstream venous pressure P_{ve}.

B Calibration metrics

This section details the objective function terms cited in Section 2.5.3. The total data misfit $\mathcal{J}_{\text{data}}$ is computed using a weighted combination of amplitude, shape, and peak accuracy, with weights empirically set to $w_{\text{MAE}} = 1.2$, $w_\rho = 0.1$, and $w_{\text{peak}} = 0.8$.

- **Normalized MAE:** To ensure scale invariance, the mean absolute error is normalized by the interquartile range (IQR) of the target signal (or the full range if the IQR is degenerate):

$$\text{nMAE} = \frac{\frac{1}{N}\sum_i |k_{\text{act}}(x_i) - k_{\text{target}}(x_i)|}{\text{IQR}(k_{\text{target}})}. \tag{33}$$

- **Shape Correlation (ρ):** The shape agreement is measured using the Pearson correlation coefficient. Letting $\tilde{k}(x_i) = k(x_i) - \bar{k}$ denote the deviation from the mean:

$$\rho = \frac{\sum_i \tilde{k}_{\text{act}}(x_i)\, \tilde{k}_{\text{target}}(x_i)}{\sqrt{\sum_i \tilde{k}_{\text{act}}(x_i)^2}\sqrt{\sum_i \tilde{k}_{\text{target}}(x_i)^2}}. \tag{34}$$

- **Peak Amplitude Error:** To ensure the maximum contractile force is captured, we penalize the difference between the modeled and target peak values:

$$E_{\text{peak}} = |k_{\text{peak,model}} - k_{\text{peak,target}}|. \tag{35}$$

Table 4: Key parameters of the 0D-EM model. Unless stated otherwise, parameters are shared between left and right ventricles; (R_0, d_0) differ between ventricles.

Symbol	**Meaning**	**Units**	**Baseline value**
T	Heart period	s	0.8
α	Velocity-dependent bridge destruction	–	1.5
k_0	Single-bridge stiffness scale	Pa	10^5
σ_0	Stress scale for newly attached bridges	Pa	0.64×10^5
k_{ATP}	Attachment rate	s^{-1}	30
k_{SR}	Detachment rate	s^{-1}	30
APD	Action potential duration	s	0.30
T_d	Atrioventricular delay	s	0.12
QRS	QRS duration	s	0.085
R_0	Reference cavity radius (ventricle-specific)	m	$2.8-3.0 \times 10^{-2}$
d_0	Wall thickness (ventricle-specific)	m	$1.4-2.8 \times 10^{-2}$
ρ	Myocardial density	$\mathrm{kg\,m^{-3}}$	1070
E_s	Series elastic modulus	Pa	3×10^7
μ	Passive viscous coefficient	Pa s	70
C_1, C_2	Mooney-Rivlin parameters	Pa	10^3, 10^3
μ_c	Active viscosity	Pa s	100
K_{at}	AV valve conductance (open)	$\mathrm{m^3\,Pa^{-1}\,s^{-1}}$	9×10^{-6}
K_{ar}	Arterial valve conductance (open)	$\mathrm{m^3\,Pa^{-1}\,s^{-1}}$	1.3×10^{-5}
K_{iso}	Leakage conductance (isovolumic)	$\mathrm{m^3\,Pa^{-1}\,s^{-1}}$	10^{-37}
τ	Windkessel time constant	s	0.8
R_p	Peripheral resistance	$\mathrm{Pa\,s\,m^{-3}}$	2×10^7
Z_c	Characteristic impedance	$\mathrm{Pa\,s\,m^{-3}}$	10^7
R_{ven}	Venous resistance (systemic / pulmonary)	$\mathrm{Pa\,s\,m^{-3}}$	2.5×10^7 / 0.5×10^7
C_{ven}	Venous compliance (systemic / pulmonary)	$\mathrm{m^3\,Pa^{-1}}$	5×10^{-6} / 50×10^{-6}
P_{ven}	Reference venous pressure (systemic / pulmonary)	Pa	3200 / 1700
Δt	Time step	s	10^{-5}